

A new insight on a mechanism of airborne and underwater sound of a drop impacting a liquid surface F

Cite as: Phys. Fluids **32**, 062004 (2020); <https://doi.org/10.1063/5.0010464>

Submitted: 10 April 2020 . Accepted: 31 May 2020 . Published Online: 18 June 2020

G. Gillot, C. Derec, J.-M. G enevaux, L. Simon , and L. Benyahia 

COLLECTIONS

F This paper was selected as Featured



View Online



Export Citation



CrossMark

ARTICLES YOU MAY BE INTERESTED IN

[Direct numerical simulation of multiscale flow physics of binary droplet collision](#)

Physics of Fluids **32**, 062103 (2020); <https://doi.org/10.1063/5.0006695>

[Fluvial instabilities](#)

Physics of Fluids **32**, 061301 (2020); <https://doi.org/10.1063/5.0010038>

[Can a toilet promote virus transmission? From a fluid dynamics perspective](#)

Physics of Fluids **32**, 065107 (2020); <https://doi.org/10.1063/5.0013318>



NEW: TOPIC ALERTS

Explore the latest discoveries in your field of research

[SIGN UP TODAY!](#)

A new insight on a mechanism of airborne and underwater sound of a drop impacting a liquid surface

Cite as: Phys. Fluids 32, 062004 (2020); doi: 10.1063/5.0010464

Submitted: 10 April 2020 • Accepted: 31 May 2020 •

Published Online: 18 June 2020



G. Gillot,^{1,2} C. Derec,³ J.-M. Génevaux,² L. Simon,²  and L. Benyahia^{1,a)} 

AFFILIATIONS

¹Institut des Molécules et Matériaux du Mans (IMMM), UMR 6283 CNRS – Le Mans Université, 1, Avenue Olivier Messiaen, 72085 LE MANS cedex 9, France

²Laboratoire d'Acoustique de l'Université du Mans (LAUM), UMR CNRS 6613, Institut d'Acoustique-Graduate School (IA-GS), 72085 LE MANS cedex 9, France

³Matière et Systèmes Complexes, Université de Paris, CNRS UMR 7057, F-75013 Paris, France

^{a)} Author to whom correspondence should be addressed: Lazhar.Benyahia@univ-lemans.fr

ABSTRACT

We report on an experimental study of the impact of a water drop on a liquid surface in the regime of the so-called *irregular entrainment*. The hydrodynamics of the phenomenon has been correlated finely to the features of the acoustic signal, both underwater and in the air, thanks to the synchronization of images and sounds in a home-made setup. If the origin of the acoustic signal is known to be caused by the capture of a bubble during the hydrodynamic flow following the impact, for the first time, a new mechanism responsible for the formation of the air bubble is highlighted. The latter is caused by the closing, like a liquid zipper, of the cavity induced by the retraction of the Rayleigh jet, by a secondary droplet detached from this jet. The comparison of the experimental data with the Minnaert model and plane wave theories reveals: (i) the time-dependence of the instantaneous oscillation frequency, (ii) a dominant frequency about 30% higher than the Minnaert prediction, (iii) a higher damping characteristic time, and (iv) a two orders of magnitude higher water–air transmission coefficient. All these results can be explained by the proximity of the bubble to the air–water interface, and by the too small dimensions of the tank to avoid underwater echoes in the measured underwater signal.

Published under license by AIP Publishing. <https://doi.org/10.1063/5.0010464>

I. INTRODUCTION

Besides producing a fascinating hydrodynamic ballet, a drop impacting a liquid surface generates a highly distinguishable sound. It is well known that the sound produced by a falling drop on a liquid surface strongly depends on the formation or not of an entrapped bubble.^{1,2} Indeed, after the impact, an open-air cavity develops inside the liquid until it reaches a maximum size and then retracts while a liquid jet arises above the liquid surface.³ The latter destabilizes into *secondary droplets*, which in turn impact the disturbed liquid surface. At different stages of this process and through several mechanisms, a bubble could be entrapped inside the liquid, producing the characteristic noise of a dripping faucet.⁴ Even if this topic has mainly been approached by fundamental studies, the potential applications that can result from

understanding this phenomenon are quite varied, such as climatic measurements,⁵ analysis of underwater events,⁶ or sound synthesis.⁷

All this process, and in particular the entrapment or not of a bubble, strongly depends on the initial drop diameter d and its speed v at the impact. A state diagram in d – v coordinates has been proposed by Pumphrey *et al.*,^{8,9} suggesting different regimes for bubble formation (BF). Probably the most well-known one, called *regular entrainment*, is observed for small drops and low impact speed. It has been investigated by several authors^{10–13} who all showed that a small bubble is created through a pinching mechanism just before the retraction of the cavity.

At higher speed and for bigger drops, another area for bubble formation appears in the d – v diagram. Already observed by Franz¹ and mentioned by Leng,¹² it is designed as an *irregular entrainment*

regime.^{8,10} Thus, the bubbles are formed later in the process, in an irregular way by detaching from a second cavity appearing after the collapse of the liquid jet, which coincides with the detachment also of a secondary drop. It is worth mentioning that this area has attracted less attention from researchers and its mechanisms are not yet described in the literature.

In the past few years, there has been growing interest in measuring the related acoustic signals to get a deeper insight into fast hydrodynamical events, such as bubble bursting.^{14,15} As for the concern, synchronizing acoustic records and image captures, some authors^{1,10,16} confirmed that the bubble apparition is accompanied by an intense acoustic signal, where the dominant frequency is linked to the radius of the bubble following Minnaert theory.¹⁷ However, only a few acoustic results have been reported yet in both air and water.^{10,18,19} It appears that the microphone signal is similar to that of the hydrophone, except that its amplitude is unexpectedly high and some physical events seem to be absent.

In this article, we present a fundamental study of a droplet falling on a liquid surface. The project aims to suggest a new analysis of the physics of this phenomenon. The perfect synchronization of acoustic signals in water and air with the associated hydrodynamic flows has allowed us to finely relate four hydrodynamic events to their acoustic signature and to understand, in particular, the differences between the acoustic signals in water and in air.

More specifically, by setting the conditions at the frontier of the so-called *irregular entrainment* regime, we have shown that the phenomenon responsible for the entrapment of the air bubble, at the origin of the acoustic wave, is completely new and is highly reproducible and regular although the details of the flow may fluctuate from one experiment to another. The latter, similar to a liquid zipper, occurs when a drop detached from the Rayleigh jet closes the subsidiary cavity. A thorough study of the acoustic signals reveals the time-dependence of the instantaneous frequency with a dominant frequency higher than Minnaert prediction, a damping and an amplitude of the acoustic signal that do not match the predictions of the existing models. We suggest that all these features can be understood by taking into account the dimensions of the tank and especially the proximity of the bubble to the air/water interface.

II. MATERIALS AND METHODS

The water drop is created by a PhD Ultra syringe pump, equipped with a 60 ml syringe ended by an Interchim Teflon cylindrical hose, usually used for chromatography analysis, with an interior and exterior diameter of 1 mm and 1.5 mm, respectively. The syringe pump flow rate is set to 10 ml/h, and thus, the diameter of the created droplet is 3.70 ± 0.05 mm. The tank and the syringe are filled out with distilled water, unless otherwise specified.

Pressure signals are recorded both underwater, by a Brüel and Kjær Type 8103 hydrophone, and in the air, by a G.R.A.S. Type 40BP 1/4 in. microphone. The hydrophone is located at 5.3 cm and the microphone at 6.4 cm from the impact location. The hydrophone is connected to a conditioning amplifier Brüel and Kjær Type 2692-0S4. The microphone is connected to a G.R.A.S. Type 26AC 1/4 in. preamplifier, linked to a conditioning amplifier Brüel and Kjær Type 2690. Both signals, recorded by a digital oscilloscope

Picoscope 4262 with a sampling rate of 500 kHz, are treated to reduce the noise by an algorithm based on spectral subtraction of the recorded ambient noise from the signal.

A video of the impact is recorded by a high-speed camera Photron FastCam SAX2 equipped with a Sigma Macro 105 mm lens. A led-based backlight is used to shine the experiment. The sample rate of video acquisition is set at 20 000 fps, unless otherwise specified. A spherical object of known dimensions is used to determine the magnification and to check that the image is not distorted.

The different acquisitions are triggered by an XCSOURCE TE174 infrared sensor module, linked to an Arduino Mega card. The module is situated just underneath the hose to detect the droplet when it detaches. All the acoustic signals are synchronized to the video footage. So, both signals are shifted with respect to time to account for the propagation times of acoustic waves from the impact point to the microphone and the hydrophone. The origin of time corresponds to the moment when the droplet touches the water surface.

The drop falls into a glass tank with external dimensions of $341 \times 165 \times 218$ mm³ and 3.4 mm thick walls. It is filled with distilled water, up to its maximum height (218 mm). It is supported by four blocks of solid polymer foam to avoid vibration transmission between the tank and the metallic structure, which allows us to keep a fixed position between the different measurement campaigns. The structure is placed in a semi-anechoic room to avoid any acoustical reflections in the air for frequencies higher than 100 Hz. The room is located in the underground floor, so the temperature, even not controlled, is almost constant and is around 19 °C. The height of fall of the drop is fixed at 76.5 cm. Thus, the velocity of the falling drop is about 3.34 ± 0.01 m/s as determined by tracking its trajectory on the video footage. Each measure is launched after the water surface is calm. Each measurement is repeated at least 50 times to quantify the repeatability of the acoustic signals and video movies.

III. RESULTS AND DISCUSSION

A. Hydrodynamic and acoustic investigation of the events leading to a new mechanism of bubble entrapment

Typical acoustic signals following the drop impact are presented in Fig. 1. The top and bottom signals correspond to the air and underwater pressures, respectively. We identify four main events. The time $t = 0$ is arbitrary fixed at the moment when the drop touches the surface of the liquid. The *First Impact (FI)* begins at $t = 0$ ms and ends around 40 ms with the appearance of the *Rayleigh Jet (RJ)*, which is the second event. The instability of the Rayleigh jet involves the detachment of *secondary drops* during its collapse. The third event, called *Bubble Formation (BF)*, first consists of the creation of a second air cavity from 140 ms approximately until it is suddenly closed by a secondary drop at 150 ms, creating an air bubble. Subsequently, the sudden closure of the cavity, which characterizes the beginning of the fourth event, causes an acoustic signal that gradually subsides over time and cohabites with the *Bubble Dynamic (BD)*. In the following, the acoustic and hydrodynamic features of these four events are precisely detailed.

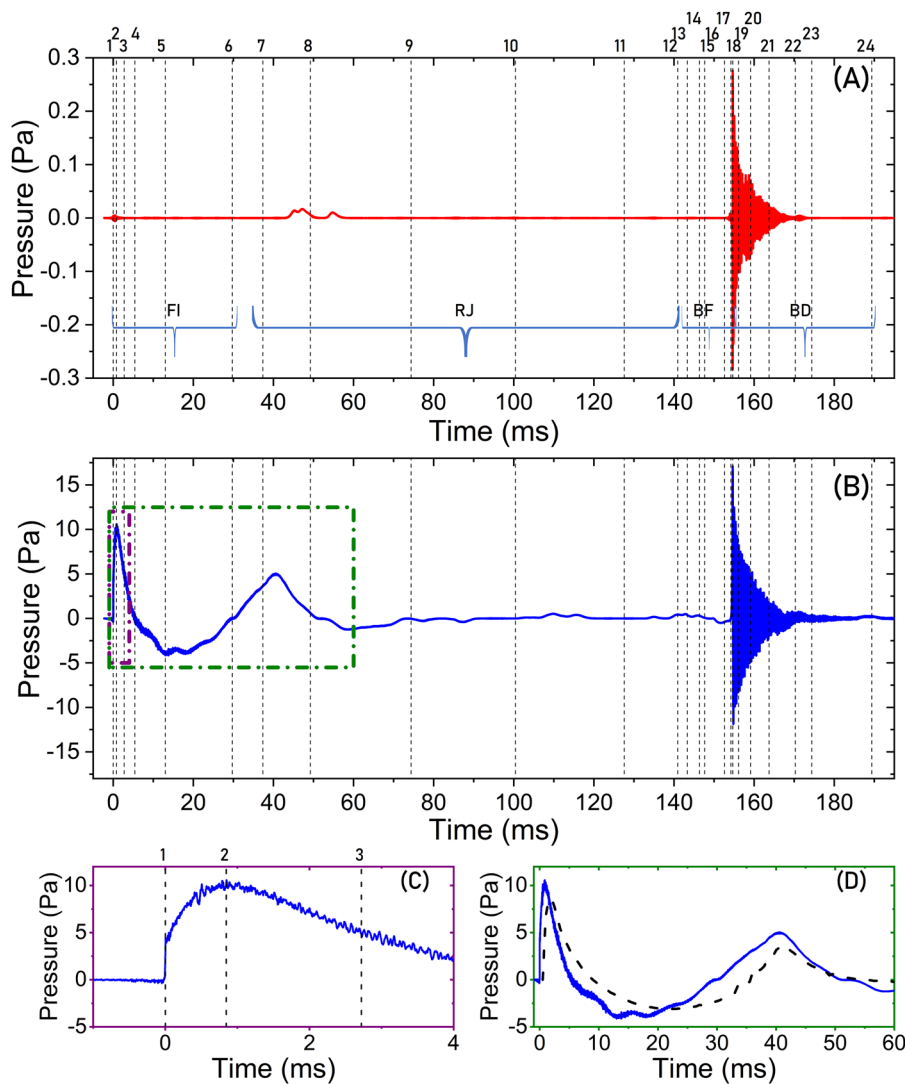


FIG. 1. (A) Signal recorded by the microphone. (B) Signal recorded by the hydrophone. Time $t = 0$ s is taken when a drop impacts the water surface. Dotted lines represent the times at which the images of Figs. 2–5 and 8 are taken. From the left to the right, four main events are identified: the First Impact (FI), Rayleigh Jet (RJ), Bubble Formation (BF), and Bubble Dynamic (BD) events. (C) A zoom at the beginning of the FI event, given by the purple box on (B), with markers 1, 2, and 3 corresponding to the images of Figs. 2 and 3. (D) A comparison between the beginning of the measured hydrophone signal and a fluid mechanics simulation (dashed line) of the hydrodynamic pressure during the first hundredth of seconds after a drop impact, given by the green box on (B).

1. First impact (FI)

The first event begins with the initial impact of the water drop on the water/air interface (event FI in Fig. 1) and lasts about $t = 40$ ms. First, an air cavity develops inside the liquid until it reaches its maximum size, and then retracts while the Rayleigh jet emerges above the interface. Note that, for lower impact energy, a bubble may be pinched during the retraction of the cavity, as described by numerous authors.^{1,8–12,19} This pinching mechanism (called “regular entrainment” in Ref. 8) is not observed in the configuration of this study.

The images related to this event are displayed in Figs. 2 and 3 with the corresponding times (1–6) on the acoustic signals (Fig. 1). On the hydrophone, the impact induces slow pressure variations but with a large amplitude. On the microphone, the signal amplitude is much weaker than the hydrophone one. At the moment of the impact (image 1), a sharp overpressure is generated in water [see

Fig. 1(C)]. As the drop merges with the liquid (image 2), the pressure continues to rise until a maximum. Then, a liquid crown develops above the surface while an air cavity develops underwater (images 2–5). During this stage, a depression is recorded by the hydrophone. When the crown and the cavity are around their maximum size (image 5), a minimum in pressure on the hydrophone signal is measured, then the crown collapses, the cavity retracts (image 6), and the underwater pressure rises until a maximum. This maximum of pressure corresponds to the beginning of the development of the Rayleigh jet.

In parallel, numerical simulations are performed. We use the open source software OpenFoam with interFoam solver that solves the Navier–Stokes equation considering incompressible fluids. The details of the simulations are based on the work reported by Castillo-Orozco *et al.*,²⁰ which we had just adapted to our case. Using axisymmetric conditions, the impact of a water drop on a water surface is defined, imposing the same drop diameter and impact velocity as

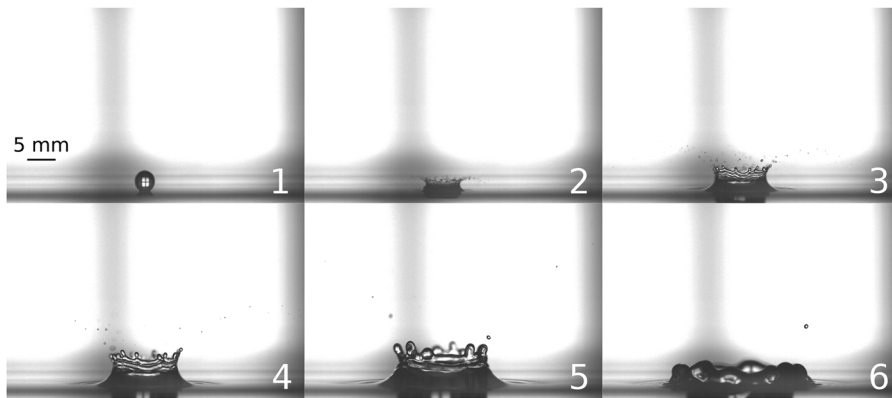


FIG. 2. Hydrodynamic flow above the water surface for the First Impact (FI) event. The marks are the same as reported in Fig. 1. The images are taken at (1) $t = 0$ s, (2) $t = 0.84$ ms, (3) $t = 2.72$ ms, (4) $t = 5.41$ ms, (5) $t = 12.99$ ms, and (6) $t = 29.72$ ms.

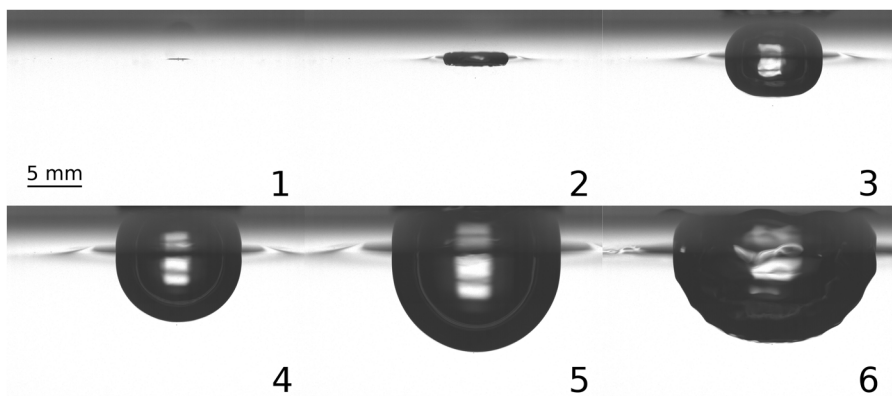


FIG. 3. Hydrodynamic flow under the water surface for the First Impact (FI) event. The images are taken at (1) $t = 0$ s, (2) $t = 0.84$ ms, (3) $t = 2.72$ ms, (4) $t = 5.41$ ms, (5) $t = 12.99$ ms, and (6) $t = 29.72$ ms.

in the experiments. The volume of fluid (VOF) method is used to deal with the interface dynamics.²¹ The hydrodynamic pressure in water during the impact is calculated at the same location of the hydrophone in the experiments. It appears that the numerical predictions are in good agreement with the measurements without any adjustable parameter [see Fig. 1(D)]. Results can be improved by further refining the mesh and taking into account the finite size of the hydrophone membrane of about 6 cm^2 .

2. The Rayleigh jet (RJ)

Between 40 ms and 140 ms (Fig. 1), the Rayleigh jet development and its collapse, designed as a Rayleigh Jet (RJ) event, happens. It does not show a noticeable signature on both hydrophone and microphone acoustic signals. The corresponding images are given in Fig. 4. At $t = 40$ ms, the cavity developed after the impact starts to retract due to surface tension and gravity, while a Rayleigh

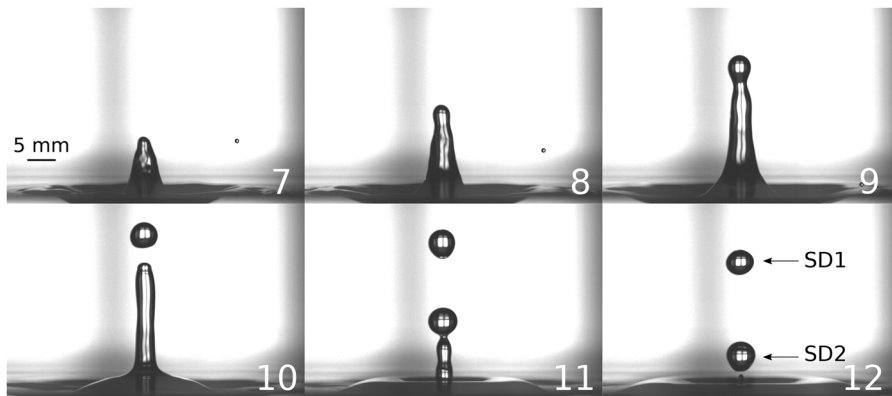


FIG. 4. Hydrodynamic flow above the water surface for the Rayleigh Jet (RJ) event. The images are taken at (7) $t = 37.37$ ms, (8) $t = 49.21$ ms, (9) $t = 74.38$ ms, (10) $t = 100.39$ ms, (11) $t = 127.58$ ms, and (12) $t = 140.94$ ms.

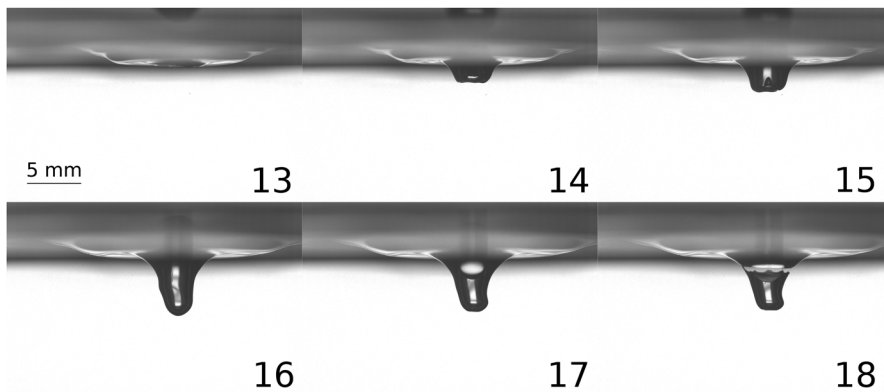


FIG. 5. Hydrodynamic flow under the water surface for the bubble formation (BF) event. The images are taken at (13) $t = 143.34$ ms, (14) $t = 146.37$ ms, (15) $t = 147.65$ ms, (16) $t = 152.62$ ms, (17) $t = 154.21$ ms, and (18) $t = 154.65$ ms.

jet emerges above the surface (images 7–9). The converging flow under the cavity creates the jet and corresponds to a decrease in underwater pressure. When the jet reaches its maximum height, Rayleigh instabilities take place and lead to the detachment of two secondary droplets (images 10–12) at variable heights of the jet. In the following, we call SD1 the first detached droplet and SD2 the second one. The remaining jet continues to collapse. Images 10–12 show how the distances between the jet column and the detached droplets increase since the surface tension and the gravity act on the column while only the gravity acts on the secondary droplets.

3. The bubble formation (BF): Liquid zip-like flow mechanism

The third event leads to a bubble formation (BF), which has both an acoustic and a hydrodynamic signature. As shown in images 13–16 of Fig. 5, the base of the remaining Rayleigh jet creates an air cavity by collapsing into water. This cavity is further closed by the first arriving droplet (SD2) (image 17) thus trapping an air bubble (image 18). The closing of the cavity by this droplet can be considered as a liquid zip-like flow, lasting about 0.15 ms, between images 17 and 18. The closing of the interface is undoubtedly faster than

the rising of the bottom of the cavity to drive out the air. As a consequence, a pocket of air remains trapped. We get a more detailed description with a 40 000 fps movie. Selected images are shown in Fig. 6. The cavity closing begins when SD2 touches the interface at one edge of the cavity (dashed red circle in image 17-b) and starts to merge with the liquid around the cavity. This merging at the top of the cavity thus propagates like a zip-process along the periphery of the cavity (images 17-c to 17-e). The detachment of the bubble is clearly reflected by the gray line crossing the cavity. The free surface is then rather at rest when the second droplet (SD1) arrives a few tens of milliseconds after.

The acoustic signal of the hydrophone shows that the pressure rises during the liquid zip-like flow mechanism until a maximum when a complete detachment of the bubble happens (see image 17-f in Fig. 6 and the marks in Fig. 7). On the contrary, the microphone signal shows first a decrease in the pressure during the liquid zip-like flow mechanism, followed by an instantaneous high pressure at the end of the liquid zip-like mechanism. Considering several impacts, the microphone signal is rather variable and depends on the accurate delay between the secondary droplet SD2 and the remaining Rayleigh jet retraction. As shown in Fig. 7, a horizontal shift (t_0) of the curves along the time axis is made, reveals that the depressions follow the same exponential curve, and the overpressure levels

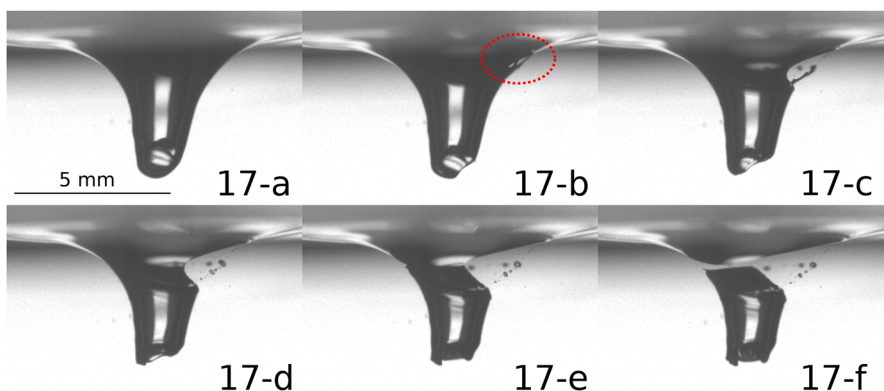


FIG. 6. Detailed images of the detachment of the air bubble (BF) and the evolution of the liquid zip-like flow mechanism. The times for each image are presented in Fig. 7. The dashed red circle shows the moment when SD2 touches the interface at one edge of the cavity. The images are taken at (17-a) $t = 152.25$ ms, (17-b) $t = 152.43$ ms, (17-c) $t = 152.59$ ms, (17-d) $t = 152.73$ ms, (17-e) $t = 152.84$ ms, and (17-f) $t = 152.89$ ms.

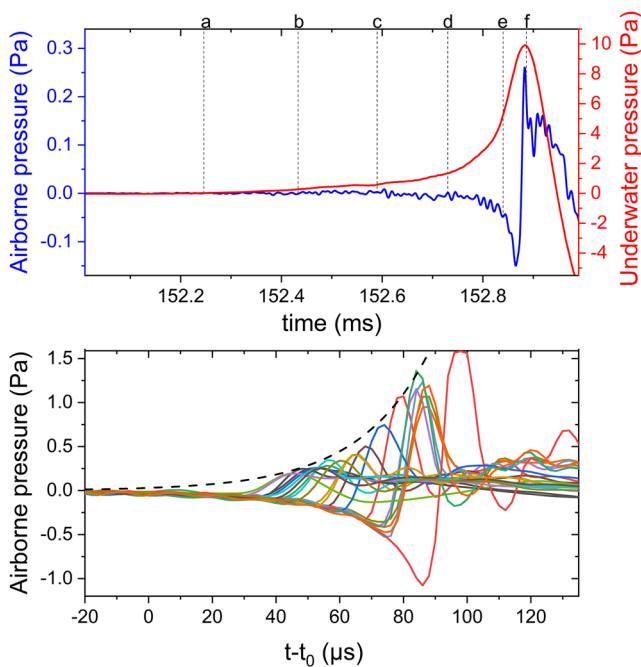


FIG. 7. Top: airborne and underwater acoustic signals during the bubble creation. Markers on the acoustic signals indicate the time when each video frame of Fig. 6 was taken. Bottom: superposition of microphone patterns by an arbitrary lag time t_0 for different measurements during the liquid zip-like flow mechanism, preceding of the intense damped sinusoidal signal. The dashed line is an exponential curve that circumscribes the maxima of the airborne pressure just at the closure of the cavity.

are circumscribed under an exponential curve too (drawn in dashed line). In addition, the ratio between these two extrema remains approximately constant for all the events. The last point concerns the difference between the time lags between these two extrema, which remains invariable for all the recorded experiments and lasts around $15 \mu\text{s}$. Note that the larger is the relative speed between the bottom of the cavity and the droplet SD2 at the impact, the higher is the maximum of the pressure.

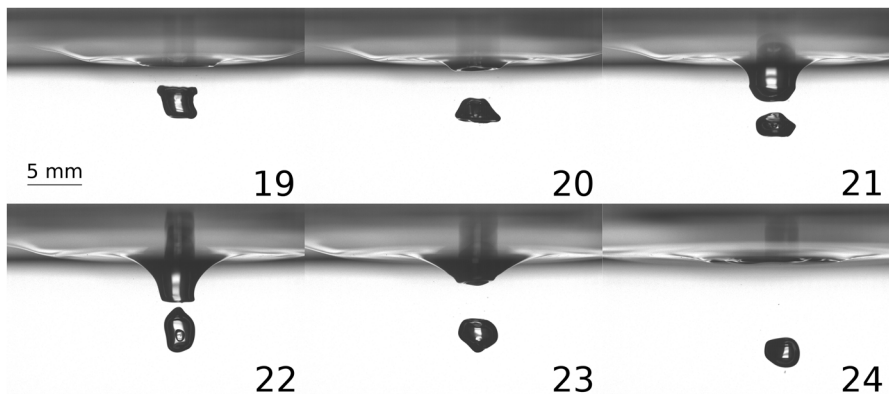


FIG. 8. Images corresponding to the evolution of an air bubble and the water interface after the formation of the bubble (BD). The images are taken at (19) $t = 156.14 \text{ ms}$, (20) $t = 159.11 \text{ ms}$, (21) $t = 163.73 \text{ ms}$, (22) $t = 170.26 \text{ ms}$, (23) $t = 174.42 \text{ ms}$, and (24) $t = 189.38 \text{ ms}$.

4. The bubble dynamic (BD)

The sudden detachment of the bubble corresponds to the beginning of the fourth event called Bubble Dynamic (BD) event. The images are given in Fig. 8. In the first moments, the bubble moves away from the interface while oscillating (images 19 and 20), and then the cavity caused by the impact of SD2 tends to approach this bubble (images 21 and 22), before finally moving away from it (images 23 and 24).

The maximum pressure when the bubble is detached, visible on the underwater and airborne signals, is followed by damped sinusoidal oscillations [Figs. 1(A) and 1(B)], which correspond to the sound which is heard, in fact, around 150 ms after the initial drop has touched the water surface. The damped underwater and airborne signals have the same dominant frequency, which depends on the bubble radius, as predicted by Minnaert.¹⁷ Nevertheless, a thorough analysis of these acoustic signals reveals some rather sophisticated and unexpected features. This is the subject of Sec. III B.

B. Analysis of the acoustic signal of the oscillating bubble

1. The frequency of the bubble oscillation

The Minnaert model describes the volume oscillations of a spherical bubble in an infinite medium.¹⁷ The natural frequency f_M of a bubble with a radius R_0 is

$$f_M = \frac{1}{2\pi R_0} \sqrt{\frac{3\gamma P_0}{\rho}}, \quad (1)$$

where γ is the ratio of specific heat of the gas inside the bubble, P_0 is the hydrostatic pressure, and ρ is the density of the fluid. As can be seen, the natural frequency of the bubble is inversely proportional to its radius.

a. Time-dependence of the frequency. The time variation of the frequency of the damped sine of the underwater acoustic signal is shown in the spectrogram in Fig. 9. The spectrogram is measured with a sliding window of 2048 points (corresponding to 4.1 ms), exhibiting an information mainly concentrated around the so-called instantaneous frequency. The instantaneous frequency appears to

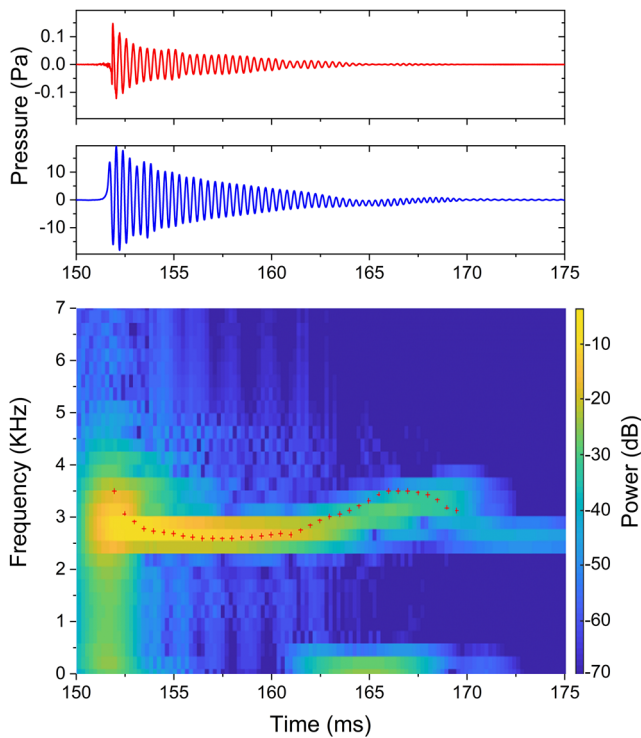


FIG. 9. Top: graphs of the temporal evolution of the pressure measured by the microphone (red) and hydrophone (blue). Bottom: time–frequency representation of the damped oscillations of the underwater pressure produced by a bubble formed after a drop impact. Red dots represent the computed frequency predicted when applying the Strasberg corrections.

change during the oscillations of the signal. During the first milliseconds, the frequency decreases rapidly, then remains constant for several milliseconds, and often finally rises at the end of the oscillations.

On the basis of video observations, the shape of the bubble and its distance to the water/air interface change continuously. According to Strasberg,²² the resonance frequency of a bubble actually depends on its deformation and on its distance to the interface. It may be corrected as follows:

$$f_s = (c_e \cdot c_d) f_M, \quad (2)$$

$$c_e = \left(\frac{e^{2/3}}{\sqrt{e^2 - 1}} \arctan \sqrt{e^2 - 1} \right)^{-1/2}, \quad (3a)$$

$$c_d = \left(1 - \frac{R_0}{2d} - \left(\frac{R_0}{2d} \right)^4 \right)^{-1/2}, \quad (3b)$$

where c_e and c_d , given by Eq. (3), are the correction coefficients due to the deformation of the bubble and to the proximity to the interface, respectively. R_0 is the bubble radius at rest, d is the distance between the center of the bubble and the interface, and e is the ratio of the major axis to the minor axis considering the deformed

bubble as an ellipsoid. It appears that, as the distance between the bubble and the interface is smaller, the corrective coefficient c_d is higher.

A tracking algorithm has been developed to follow the evolution of the bubble position and shape during its oscillations. From these measurements, Strasberg correction coefficients can be calculated for each frame and applied to the theoretical Minnaert frequency considering a bubble radius measured on the images when the bubble is at rest.

The instantaneous frequency is then corrected according to this concept and plotted on the graph. The results show both qualitative and quantitative agreement, which we will detail in Sec. III B 1 b. In particular, the occurrence of the frequency at the end of the oscillations, reported elsewhere,⁷ is due to a strong decrease in the distance between the bubble and the interface, caused by the impact of SD2 (see images 20–22 in Fig. 8).

b. Comparison to Minnaert frequency. For each pressure oscillation of the underwater acoustic signal, the dominant frequency f_d is calculated by taking the maximum of the Fourier transform over the entire oscillating signal (see example in Fig. 9). On the other hand, the tracking algorithm, as described above, allows us to determine the average coefficients \bar{c}_d and \bar{c}_e . Then, we use them to calculate the corrected frequency f_c [Eq. (4)],

$$f_c = f_d \frac{1}{\bar{c}_d \cdot \bar{c}_e}. \quad (4)$$

Figure 10 compares f_M to f_c . Error bars correspond to the minimum and maximum frequencies calculated, from the maximum and minimum distances and deformations measured during the volume oscillation of each bubble. After the correction, the measurements are in very good agreement with Minnaert theory. It is worth mentioning that, in the conditions of this study, the correction due to the bubble deformation is small compared to the correction due to its distance from the air/water interface (see the inset in Fig. 10).

2. Air–water transmission

For a plane wave traveling from water to air, the pressure transmission coefficient is given by $T = \frac{2Z_{air}}{Z_{air} + Z_{water}}$, with $Z_{air} \sim 4 \times 10^2 \text{ Pa s m}^{-1}$ and $Z_{water} \sim 15 \times 10^5 \text{ Pa s m}^{-1}$, the impedances, respectively, of air and water, predicting a transmission around 5×10^{-4} . For these measurements, the hydrophone is situated at 4 cm horizontally from the impact point, and 3.4 cm vertically. The microphone is situated 6 cm horizontally, and 2.1 cm vertically from the impact point. The water-to-air pressure transmission is roughly constant and equal to 10^{-2} (see, for example, acoustic signals in Figs. 1 and 9). This value is roughly the same as the one reported by Phillips *et al.*¹⁹ They explained the unexpected transmission value by the oscillation of the water surface. However, we prove here that this high transmittance value is essentially a consequence of the proximity between the bubble (source of the acoustic signal) and the interface.

The entrapped bubbles usually produce oscillations at frequencies mainly between 2 kHz and 10 kHz, corresponding to wavelengths λ between 15 cm and 75 cm in water, which is much larger than the bubble–interface distance of about a few millimeters. Thus, the acoustic signal arriving on the interface cannot be considered as

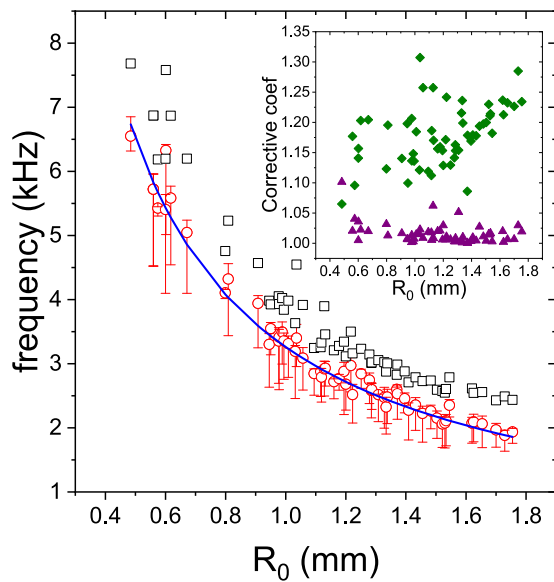


FIG. 10. The measured dominant frequencies f_d (black squares) as a function of the bubble radius at rest (R_0), and the corrected frequencies f_c (red circles) accounting for the bubble/interface distance and the anisotropy of the bubbles. The blue solid line is the prediction of the Minnaert model with the radius R_0 . The inset represents the Strasberg coefficients, c_e (green diamonds) and c_d (purple triangles), calculated from the movies for each case.

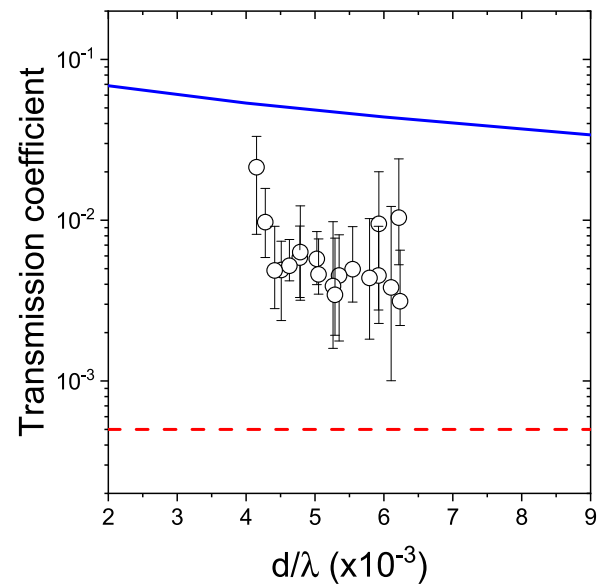


FIG. 11. Transmission coefficient through the water–air interface as a function of the ratio of the distance between the acoustic source to the interface and the wavelength of the acoustic wave in the water. The circles correspond to the experimental measurements, and the solid line is the theoretical prediction accounting for the geometry of the acoustic source and the distance to the interface. The dashed line is the transmission coefficient given by the plane wave theory.

a plane wave, and one must consider the geometry features of the problem, i.e., a spherical source and a planar interface. So, a spherical wave may be described as an infinite sum over frequencies of monochromatic plane waves, and in this situation, this sum contains evanescent waves.²³ Due to the proximity of the source and the interface, evanescent waves in water can reach the interface and produce propagative waves in the air (as Z_{air} is much smaller than Z_{water}). Theoretical studies have shown that this effect leads to a large increase in the acoustic energy transmitted to the air.^{23–25}

Numerical simulations based on the finite element method (using Comsol Software, acoustics module) have been computed to predict the transmission coefficient in our experimental conditions. Using axisymmetric geometry, a water–air interface is simulated. A monopolar source is defined just below the interface. As the transmission coefficient should depend on the ratio of the source–interface distance over the wavelength, it is chosen to fix the frequency at 3 kHz and to vary the source–interface distance. Perfect matching layers are used to simulate a semi-infinite medium both in water and in air. The pressure calculations in the air and in water are performed at the same locations as the microphone and hydrophone in the experimental setup. The results, shown in Fig. 11, display an increase in the transmission coefficient when the ratio of the distance of the interface to the wavelength decreases.

The experimental transmission coefficients are measured. For each bubble oscillation, the pressure values of the extrema of the oscillating signal for both microphone and hydrophone are measured, and the ratio is calculated. Note that this method allows us to follow the temporal evolution of the transmission coefficient, which varies with time. This can be explained by the variation of

the bubble–interface distance during the oscillations. In order to compare with the simulation, a mean transmission coefficient is calculated, as well as a mean bubble–interface distance, measured on the video footage.

The results are plotted in Fig. 11. The error bars display the maximum and minimum values for both the distance and the transmission coefficient. The measured pressure ratios are of the same order of magnitude as the simulation, although slightly lower. This effect may be explained by the tank influence on the acoustic field in water. Although the simulations are performed for a semi-infinite medium, the pressure measured by the hydrophone is the sum of the direct source radiation and the reflected radiation on the tank walls, and the measured transmission coefficient is then underrated. The role of the reflections on the tank walls is clearly attested in Sec. III B 3.

3. Damping

We now focus on the apparent damping of both underwater and airborne acoustic signals. The experimental damping time τ of each signal (τ_{water} and τ_{air} measured in water and in air, respectively) is calculated by measuring the evolution in time of the extrema of each signal and fitting them by an exponential decrease of characteristic time τ . For several experiments, bubbles of various sizes and so various oscillation frequencies are produced, and the damping times are measured for each case. As shown in Fig. 12, τ_{water} is clearly larger than τ_{air} for any frequency.

For a bubble in an infinite medium (i.e., far from both the free surface and the tank walls), the dimensionless damping constant δ defined by $\delta = 2/\omega_0\tau$ is due to three origins,²⁶

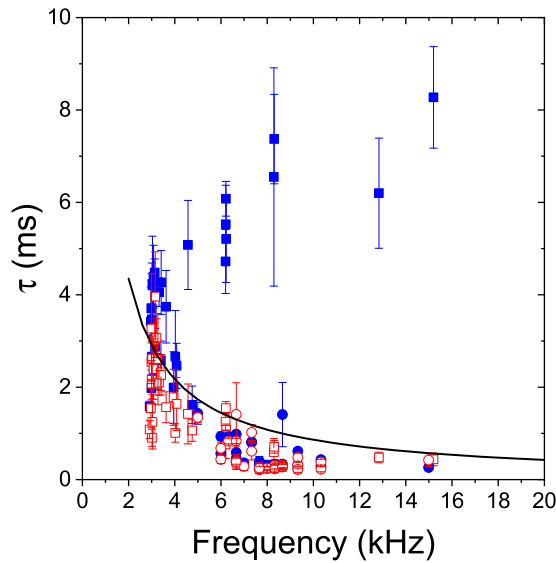


FIG. 12. Characteristic damping time τ of the oscillating signals measured in water (blue closed symbols) and in the air (red open symbols). Measurements performed both in a tank (square symbols) and in a big swimming pool (circle symbols) are compared to the theoretical predictions (solid line).

$$\delta = \delta_{rad} + \delta_{th} + \delta_{vis}, \quad (5)$$

with ω_M being the natural bubble pulsation, and δ_{rad} , δ_{th} , and δ_{vis} describing the radiation damping, thermal damping, and viscous damping, respectively. These three different quantities are expressed as²⁶

$$\delta_{rad} = \frac{\omega_M R_0}{c}, \quad (6a)$$

$$\delta_{vis} = \frac{4\eta}{R_0^2 \rho \omega_M}, \quad (6b)$$

$$\delta_{th} = \frac{P_0 \text{Im}(\phi)}{R_0^2 \rho \omega_M^2}, \quad (6c)$$

with c being the celerity of longitudinal acoustic waves in the liquid, η the shear viscosity, ρ the density of the liquid, and $\phi = 3\gamma \left(1 + 3i \frac{(\gamma-1)l_d}{\sqrt{2}R_0}\right)$ in the adiabatic limit ($l_d \ll R_0$), with l_d being the thermal diffusion length. As shown in Fig. 12, the values of the damping time obtained by this model are in satisfactory agreement with those of the experimental damping time measured in the air but far from the values measured in water.

To identify a possible role of the tank walls in the signal measured by the hydrophone, experiments were performed in a real pool of dimensions $10 \times 25 \times 2.2 \text{ m}^3$. In these conditions, the measured τ_{water} and τ_{air} are similar and consistent with the theoretical values (see Fig. 12). In the pool, the working area (impact point and hydrophone) is at 2.2 m of the closest wall, in order to maximize the time lag between the direct signal and the first reflection on the wall (the reflection from the interface cannot be avoided). The first echo is therefore supposed to be measured on the hydrophone after about

3 ms, which is higher than the characteristic damping time of most bubbles.

This result suggests that the hydrophonic signals obtained in a tank are made up of the acoustic emission of the bubble and all the reflections on the walls of the tank. Moreover, the amplification at a given frequency depends on the frequency resonance of the water volume. However, the damping time deduced from the microphone measurements is not influenced by the liquid container. Indeed, the microphone measures the direct field of the source, without the reflections on the container walls.

IV. CONCLUSION

This work reports on the hydrodynamics and acoustics, below and above the water surface, of a drop of water impacting the liquid surface at the frontier of the so-called *irregular entrainment* regime. The synchronization of the images obtained by a fast camera and the acoustic signals allowed a very fine and novel description of the phenomenon.

During the first hundredth of seconds, the hydrophone signal shows a relatively slow variation in pressure associated with the development of an air cavity following the impact. At about 150 ms after the impact, an intense acoustic signal is recorded both under water and in the air. It corresponds to the free oscillations of an air bubble whose entrapment mechanism is first revealed here. Indeed, when the Rayleigh jet, induced by the retraction of the primary cavity, collapses, two secondary droplets are released. The second droplet falls back and closes the air cavity created by the retraction of the Rayleigh jet. The closing of this cavity resembles a liquid zipper and generates a specific pressure signal in the air.

Once the bubble has formed, an acoustic signal is measured in the air and under water, corresponding to the oscillations of the bubble volume, as described by Minnaert. However, the measured frequency values are about 20%–30% higher than those predicted by the Minnaert model. In addition, we have highlighted the time-dependence of the instantaneous oscillation frequency. These features are related to the proximity of the bubble to the interface and to its deformation. The corrections applied to the Minnaert theory, as proposed by Strasberg, show good agreement with the experimental results.

The transmission coefficient across the water–air interface is also studied and is more than ten times higher than the predicted one for plane waves. In contrast, the proximity of the bubble to the interface and the spherical geometry of the source may explain the increased transmission across the interface.

Finally, the comparison between measurements in a tank and in a large swimming pool shows the important role of the tank dimensions. The results highlight that the duration of the acoustic signal measured on the hydrophone is greatly increased by acoustic reflections from the tank walls.

ACKNOWLEDGMENTS

The authors would like to express their sincere thanks to Mr. James Blondeau, assistant laboratory engineer at LAUM, who efficiently and significantly contributed to the setup of the experiments.

Our thanks also go to La Région des Pays de la Loire, which financially supported this work within the framework of the Acapulcos project of the RFI LMAC.

The authors would finally like to thank the municipality of Le Mans for having allowed us to carry out two measurement campaigns in the Ardriers swimming pool, especially Mr. Laurent Hamelin, head of the sports facilities department of the city of Le Mans, Mr. Jean-Marc Loiseau, head of the pool, Mr. Cyril Compain, technical agent, and Mr. Patrick Mahoué from Le Mans Innovation.

DATA AVAILABILITY

The data that support the findings of this study are available on request from the corresponding author. The data are not publicly available due to state restrictions, such as privacy or ethical restrictions.

REFERENCES

- ¹G. J. Franz, “Splashes as sources of sound in liquids,” *J. Acoust. Soc. Am.* **31**, 1080 (1959).
- ²A. M. Worthington, *A Study of Splashes* (Longmans, Green & Co., London, New York, Bombay, Calcutta, 1908).
- ³M. Huimin, L. Changgen, L. Xu, H. Hongbo, and D. Jiaojiao, “Deformation characteristics and energy conversion during droplet impact on a water surface,” *Phys. Fluids* **31**, 062108 (2019).
- ⁴Y. D. Chashechkin and V. E. Prokhorov, “Acoustics and hydrodynamics of a drop impact on a water surface,” *Acoust. Phys.* **63**, 33 (2017).
- ⁵G. Kathiravelu, T. Lucke, and P. Nichols, “Rain drop measurement techniques: A review,” *Water* **8**, 29 (2016).
- ⁶J. A. Nystuen, S. E. Moore, and P. J. Staben, “A sound budget for the south-eastern Bering Sea: Measuring wind, rainfall, shipping, and other sources of underwater sound,” *J. Acoust. Soc. Am.* **128**, 58 (2010).
- ⁷K. van den Doel, “Physically based models for liquid sounds,” *ACM Trans. Appl. Percept.* **2**, 534 (2005).
- ⁸H. C. Pumphrey, L. A. Crum, and L. Bjorno, “Underwater sound produced by individual drop impacts and rainfall,” *J. Acoust. Soc. Am.* **85**, 1518 (1989).
- ⁹H. C. Pumphrey and P. A. Elmore, “The entrainment of bubbles by drop impacts,” *J. Fluid Mech.* **220**, 539 (2006).
- ¹⁰H. C. Pumphrey and A. J. Walton, “Experimental study of the sound emitted by water drops impacting on a water surface,” *Eur. J. Phys.* **9**, 225 (1988).
- ¹¹H. N. Oguz and A. Prosperetti, “Bubble entrainment by the impact of drops on liquid surfaces,” *J. Fluid Mech.* **219**, 143 (1990).
- ¹²L. J. Leng, “Splash formation by spherical drops,” *J. Fluid Mech.* **427**, 73 (2001).
- ¹³M. S. Longuet-Higgins, “An analytic model of sound production by raindrops,” *J. Fluid Mech.* **214**, 395 (2006).
- ¹⁴A. Bussonnière, A. Antkowiak, F. Ollivier, M. Baudoin, and R. Wunenburger, “Sound of interfacial flows: Unraveling the forces shaping fast capillary flows using their acoustic signature,” [arXiv:1810.05599](https://arxiv.org/abs/1810.05599) [cond-mat, physics:physics] (2018).
- ¹⁵G. B. Deane, “Determining the bubble cap film thickness of bursting bubbles from their acoustic emissions,” *J. Acoust. Soc. Am.* **133**, EL69 (2013).
- ¹⁶A. Prosperetti and H. N. Oguz, “The impact of drops on liquid surfaces and the underwater noise of rain,” *Annu. Rev. Fluid Mech.* **25**, 577 (1993).
- ¹⁷M. Minnaert, “XVI. On musical air-bubbles and the sounds of running water,” *London, Edinburgh Dublin Philos. Mag. J. Sci.* **16**, 235 (2009).
- ¹⁸V. E. Prokhorov and Y. D. Chashechkin, “Sound generation as a drop falls on a water surface,” *Acoust. Phys.* **57**, 807 (2011).
- ¹⁹S. Phillips, A. Agarwal, and P. Jordan, “The sound produced by a dripping tap is driven by resonant oscillations of an entrapped air bubble,” *Sci. Rep.* **8**, 9515 (2018).
- ²⁰E. Castillo-Orozco, A. Davanlou, P. K. Choudhury, and R. Kumar, “Droplet impact on deep liquid pools: Rayleigh jet to formation of secondary droplets,” *Phys. Rev. E* **92**, 053022 (2015).
- ²¹C. W. Hirt and B. D. Nichols, “Volume of fluid (VOF) method for the dynamics of free boundaries,” *J. Comput. Phys.* **39**(1), 201 (1981).
- ²²M. Strasberg, “Gas bubbles as sources of sound in liquids,” *J. Acoust. Soc. Am.* **28**, 20 (1956).
- ²³O. A. Godin, “Sound transmission through water–air interfaces: New insights into an old problem,” *Contemp. Phys.* **49**, 105 (2008).
- ²⁴E. V. Glushkov, N. V. Glushkova, and O. A. Godin, “The effect of anomalous transparency of the water–air interface for a volumetric sound source,” *Acoust. Phys.* **59**, 6 (2013).
- ²⁵A. P. Voloshchenko and S. P. Tarasov, “Effect of anomalous transparency of a liquid–gas interface for sound waves,” *Acoust. Phys.* **59**, 163 (2013).
- ²⁶T. Leighton, *The Acoustic Bubble* (Academic Press, 2012).